**Revision 2**

# The origin of trapiche-like inclusion patterns in quartz from Inner Mongolia, China

Gabriela A. Farfan,[1] John Rakovan,[2] Michael R. Ackerson,[1] Benjamin J. Andrews,[1] Jeffrey E. Post[1]

[1]Department of Mineral Sciences, Smithsonian Institution, Washington, DC, 20560

[2]Department of Geology and Environmental Earth Science, Miami University, Oxford, OH, 45056

## Abstract

Fibrous amphibole and clay mineral inclusions that form striking trapiche-like patterns within quartz crystals from Inner Mongolia, China present a challenge to uncover how these crystals grow and incorporate inclusions in a geological context. We propose that the patterns formed as a result of protogenic clay (ferrosaponite or nontronite) inclusions that were preferentially trapped on rough surfaces during quartz crystal growth. The rough surface texture of these crystals is the result of multiple growth centers during 2D nucleation and spread and split crystal formation. Observations via optical microscopy, cathodoluminescence and three-dimensional micro-CT scanning highlight how the exterior surface textures on the termination of a complete quartz crystal mimic its interior inclusion patterns. Cathodoluminescence images, as well as varying aluminum concentrations along a core-to-exterior transect in a quartz crystal slice, suggest that the formation fluid underwent a heterogeneous chemical history. Measurements of Ti and observations of fluid inclusions suggest the quartz formed at a temperature of under

348°C. This study presents the details surrounding split crystal growth in quartz in a natural geological setting, which has implications for inspiring new materials and may serve as an indicator for turbid and highly supersaturated formation fluid conditions in geological formations.

**Key Words:** split crystal growth, quartz, inclusion incorporation, trapiche-like, Huanggang deposit, micro-CT scanning

## Introduction

Quartz is the predominant mineral in continental supracrustal rocks. Colored and/or patterned quartz varieties (e.g. smoky quartz, pink rose quartz, golden yellow citrine, purple amethyst) are much sought-after as cut gems (Webster 1995) or as hand specimens for mineral collectors (Rykart 1995, Lauf 2012). During growth, quartz crystals may entrap fluids or mineral species that help unravel their growth conditions and history (e.g. Ihinger and Zink 2000). In this study, we investigated mineral inclusions in quartz crystals from the Huanggang Fe-Sn skarn deposit in Inner Mongolia, China, which are arranged in trapiche-like patterns observed in slices cut perpendicular to the quartz *c*-axis (Figure 1). This particular included quartz was first described by Laurs (2016) as being similar to quartz slices with radiating fibers described from Colombia (Krzemnicki and Laurs 2014). Star patterns in minerals have long enchanted mineralogists, gemologists, and materials scientists, with stars ranging from trapiche emeralds (Pignatelli et al. 2015), to trapiche-like patterns in quartz (Okada et al. 2017; Sun et al. 2018) and corundum (Vertriest et al. 2016), to chatoyant asterism in corundum (Nassau, 1968), to cordierite-indialite intergrowths (Sakura ishi) altered to muscovite colloquially known as cerasite or "cherry

47 blossom stone" (Rakovan et al 2006), and pinwheels of color variation in sector zoned crystals
48 (Vasconcelos et al., 1994; Rakovan 2009). All of these examples of stars form through very
49 different mechanisms, and the patterns we observe in these quartz slices from the Huanggang
50 mine are no exception. Here, we use a multi-method approach to characterize the mineral
51 inclusions and explain how the growth history of these quartz crystals led to the striking oriented
52 inclusion patterns. Understanding how crystal growth is linked to inclusion incorporation in
53 nature to form these remarkable interior patterns is a fundamental topic in mineralogy and may
54 be applicable to materials science. In this case, we suggest that the growth history of the quartz
55 crystal had a profound influence on the incorporation and formation of inclusion patterns. In
56 particular, we examine split crystal growth and two-dimensional nucleation growth mechanisms.
57 The macroscopic surface roughness associated with these two mechanisms leads to entrapment
58 and inclusion of foreign phases, and the spatial distribution of rough areas accounts for the
59 internal patterns observed.

60

61 **Geological setting**

62

63 The included quartz crystals studied here are reported as originating from the Huanggang
64 Fe-Sn skarn deposit in Inner Mongolia, China, (Laurs 2016). This deposit is known to produce a
65 plethora of minerals from the seven mines that span across an area of approximately 2.5 by 20
66 km (Wang et al. 2001; Ottens and Neumeier 2012). Many of these minerals exhibit morphologic
67 characteristics similar to the those seen in our quartz samples (Ottens and Neumeier 2012). Other
68 quartz specimens from these Huanggang Sn-skarn deposits include the aggregate "artichoke
69 quartz" habit, which are commonly included with suspected hedenbergite (in green quartz) and

This is the peer-reviewed, final accepted version for American Mineralogist, published by the Mineralogical Society of America.
The published version is subject to change. Cite as Authors (Year) Title. American Mineralogist, in press.
DOI: https://doi.org/10.2138/am-2021-7454. http://www.minsocam.org/

other minerals, as well as amethyst and inclusion-free quartz with subcrystals (Figures 73−75 in Ottens and Neumeier 2012).

## Materials and Methods

### *Sample acquisition and preparation*

The quartz crystal slices used in this study exhibited trapiche-like patterns with dark-colored and light-colored inclusions. One slice was acquired initially, followed by six more slices from the same locality that were reportedly all cut from one crystal (NMNH 177446; Figure 1). The circumferences of these slices are all bound by prism surfaces, indicating that they were cut from the main crystal below the terminating rhombohedral faces. All of these slices came pre-polished. One slice from the group of six was further sectioned into fourths to expose the inner, inclusion-rich regions of the quartz for X-ray diffraction analyses. Additionally, we acquired a complete, euhedral crystal, reported to be from Chifeng, Inner Mongolia, China (NMNH 177447; Figure 2a). Chifeng City is a municipality close to the Huanggang Fe-Sn deposit. The complete specimen was cut perpendicular to the *c*-axis, roughly in half (Figure 2a,b), with a diamond saw using water as a lubricant. This cut was made through the portion of the crystals with dark inclusions (and split subcrystals). A (001) slice was taken from the bottom of the upper half of the crystal (Figure 2b). All samples were cleaned in a sonicator with ethanol for at least 5 minutes to remove any debris before analyses were performed. One slice was carbon-coated for EPMA analyses.

### *Optical petrography*

Images of inclusions were taken on an Olympus BX51 petrographic microscope with plane-polarized light. In order to distinguish the interior growth textures of the quartz, we also photographed a subset of the quartz thick-slices between crossed polarizing filters.

***Cathodoluminescence***

Cathodoluminescence (CL) imaging was performed on a polished, uncoated section that was also used for SEM analyses. We used a Luminoscope ELM-3R mounted on an Olympus BX41 optical microscope operating at 15kV and 0.5mA with a beam diameter of approximately 2mm. Due to the low CL signal from quartz, image contrast and brightness were digitally enhanced to reveal internal growth patterns. Black and white CL images were also collected at higher spatial resolutions and magnifications using a Bruker monochromatic CL system on an electron microprobe described below.

***Elemental analyses***

Polished and cleaned surfaces of the crystal slices showing exposed pits containing dark-colored inclusions, were examined by backscattered electron (BSE) imaging using a FEI NOVA NanoSEM 600 analytical scanning electron microscope coupled with an energy-dispersive X-ray spectrometer (EDS). The samples were left uncoated and were imaged and analyzed using low-vacuum backscattered electron mode. The chamber pressure in low-vacuum mode was approximately ~100Pa and used water vapor to dissipate charge buildup. Beam voltage was ~15kV with a ~0.3nA current and a spot size of ~1μm. The Noran Ultra-dry EDS was run with a dwell time of 30s per analysis with a dead time under 20% and without mineral standards. All inclusions measured for EDS were many times larger (~5-10μm) than the spot size of the instrument.

This is the peer-reviewed, final accepted version for American Mineralogist, published by the Mineralogical Society of America.
The published version is subject to change. Cite as Authors (Year) Title. American Mineralogist, in press.
DOI: https://doi.org/10.2138/am-2021-7454. http://www.minsocam.org/

To trace the quartz growth history and chemical environment during quartz growth, we performed electron microprobe (EPMA) analyses using wavelength dispersive spectroscopy (WDS) on the JEOL 8530F (EPMA) along a transect of the trapiche-like quartz slice which was imaged with CL. We collected spot analyses across a core-to-rim transect of the quartz slice with a spot size of 10 µm and a step size of 150 µm between points. We measured Ti on 3 PET crystals and Al on 2 TAP crystals on peak for 300 s (150 s for both the upper and lower background) at 200 nA and a 15 kV accelerating voltage, using ilmenite as a standard for Ti and corundum as a standard for Al. Analyses were also performed on a set of internal standard quartz crystals with known Ti and Al concentrations (0-1200 ppm Al, 0-300 ppm Ti) which were then used to validate and correct the measured values.

***Raman spectroscopy***

Confocal Raman spectroscopy was performed on the inclusions by focusing through the quartz and onto single inclusions with a spot-size of approximately 1.5 µm using a Horiba LabRAM Evolution Raman spectrometer with a 532nm laser and a 300 groove grating, collecting data from 100–4000 $cm^{-1}$ for five seconds with four accumulations at 10% laser power per point. Preliminary phase identifications were performed by using Know-It-All software paired with the RRUFF database.

***X-ray diffraction***

XRD analysis was performed on the inclusion-rich tip of one of the quarter slices (Figure 5A, yellow circle) using a Rigaku D/Max Rapid micro-X-ray diffractometer with Mo Kα radiation (λ = 0.709300 Å) at 50kV and 40mA for 10 minutes. The diffractometer uses a curved imaging plate detector and RINT RAPID control software by Rigaku. Diffraction images were integrated into 1D patterns using 2DP Software and the non-quartz mineral phases were

identified using the search-match algorithms in Jade 9.0 using the ICDD PDF4+ Minerals (2019) database. The sample was held in a fixed position during the data collection. The resulting diffraction pattern on the imaging plate consisted of single-crystal diffraction spots from the quartz, along with faint, but distinct powder rings from the fine-grained, inclusion phases. The diffraction pattern was integrated across small angles in such a way that excluded the intense quartz diffraction spots, and only included the ring pattern data (Figure 5B, yellow triangles).

***Micro X-ray CT scanning***

To observe the detailed three-dimensional arrangement of the inclusions, we performed micro-X-ray CT scanning on the complete quartz crystal and a quartz crystal slice, utilizing a Phoenix v|tome|x m X-ray CT scanner by General Electric. Three-dimensional reconstructions were performed in Datos 3.2, with segmentation and visualization completed using Volume Graphics **3.2.4**. The complete crystal sample was scanned using the micro-X-ray tube operating at 100 kV and 100 µA, resulting in a power of 10 W on the X-ray target (these parameters optimize X-ray flux through the sample and X-ray tube longevity). The crystal was scanned for 3:32 hours with 3000 projections per position as the crystal was rotated through 360 degrees; each projection was collected with a gain of 1 and a dwell time of 500 ms. As the crystal was larger than the field of view with the desired voxel (3D pixel) resolution, the upper and lower portions of the crystal were imaged in separate scans with an overlap of 10 pixels; those images were then merged to form a single reconstruction. The resulting reconstruction had a voxel size of 20.34 µm. The same quartz slice studied with SEM was also scanned using the nano-X-ray tube operating at 110 kV and 100 µA (yielding a power of 2.9 W on the X-ray target and optimized spatial resolution and X-ray flux). 3000 projections were collected over 1:43 hours as

This is the peer-reviewed, final accepted version for American Mineralogist, published by the Mineralogical Society of America.
The published version is subject to change. Cite as Authors (Year) Title. American Mineralogist, in press.
DOI: https://doi.org/10.2138/am-2021-7454. http://www.minsocam.org/

the sample was rotated 360 degrees with a gain of 0.5 and a dwell time of 500 ms. The three-dimensional quartz slice reconstruction had a voxel size of 9.39 µm.

All mineralogical and chemical analyses were performed at the Smithsonian National Museum of Natural History in the Department of Mineral Sciences and the Scientific Imaging Laboratory.

## Results

### *Description of trapiche-like quartz*

Photographs of the trapiche-like included quartz slices closely resemble the figures published by Laurs 2016 (Figure 1). The complete quartz crystal (Figure 2a) sliced perpendicular to the *c*-axis revealed trapiche-like inclusion patterns (Figure 2b) consistent with the three-fold symmetry of the quartz structure. This particular sample is split into two large discrete quartz crystals, intergrown in sub-parallel orientation —and each showing distinct inclusion patterns that merge in the middle (Figure 2b). The overall specimen shows crystal splitting on several scales, from the splitting of the two main crystals, to smaller split subcrystals (Figure 2a, white arrows, and 2c). Splitting along the length of the specimen appears to start at the same position as the presence of the dark inclusions (Figure 2a, black arrows). This splitting has caused a ~20% increase in width from the base of the crystal (Figure 2a, yellow bars) to the top of the crystal (red bars). The prism faces of all split subcrystals are especially rough and are completely covered by even smaller subordinate crystals, with distinct terminations (Figure 2c). The orientations of the larger split subcrystals and the smaller subordinate crystals form a continuum from slightly divergent (by at least several degrees) from that of the main crystal, to being parallel to the main crystal. In the latter case, the subcrystals are distinct only in their external

183 morphology. Because they are parallel to the main crystal, they are structurally contiguous and
184 thus are not truly separate crystals. The terminations on the two main crystals show rough
185 surface texture at the centers of the rhombohedral faces where subcrystals on the faces coalesce
186 (Figure 2d, yellow arrows), and a smoother surface texture near the rhombohedral edges (Figure
187 2d, red arrows). Differences in surface roughness are clearly visible when the crystal termination
188 is viewed down the *c*-axis (Figure 2e), where white-colored clay particles are presently adhered
189 preferentially on the rough portions of crystal faces, leaving the edges clean. This perspective of
190 the termination shows the hexagonal trapiche-like pattern that mimics the patterns of inclusions
191 in our slices (Figure 1,2b). Where the two main crystal terminations meet, there are also surficial
192 white clays trapped in the reentrant, which mimic the distributions of inclusions within the slices
193 (Figure 2e, blue arrows).

194 Three-dimensional reconstructions of micro-CT scans of the quartz crystal surfaces
195 (Figure 3a) highlight the surface textures observed in the photographs in Figure 2. The surface
196 reconstruction clearly shows the transition between the rough areas at the centers of the
197 rhombohedral crystal faces (yellow arrows) and the smooth areas near the edges (red arrows) of
198 the crystal terminations (Figure 3a). The three-dimensional micro-CT scan image of the interior
199 of the quartz crystal shows phantoms (outlines of buried concentric growth zones) outlined by
200 the inclusions (Figure 3b). Micro-CT sections oriented perpendicular to the quartz *c*-axis through
201 the phantoms show the familiar trapiche-like distributions of the inclusions (Figure 3c,d,e).
202 Furthermore, 3D-rendered micro-CT images highlight the three-dimensional clay inclusion trails
203 (Figure 3c,d), which mimic the distribution of pits created by the coalescing subcrystal
204 terminations on the rhombohedral crystal faces of the main quartz crystals (Figure 3a). The
205 micro-CT scans also reveal some small voids alongside the clay inclusions (Figure 3e),

This is the peer-reviewed, final accepted version for American Mineralogist, published by the Mineralogical Society of America.
The published version is subject to change. Cite as Authors (Year) Title. American Mineralogist, in press.
DOI: https://doi.org/10.2138/am-2021-7454. http://www.minsocam.org/

206 indicating that some of the surface depressions on the former crystal terminations (Figure 3a)
207 were not completely filled-in with clays.

208 The trapiche-like patterns in the quartz slices consist of dark-colored aggregate inclusions
209 and fibrous inclusions (Figure 4). Images of the dark-colored aggregate inclusions in the quartz
210 slices reveal that they align to form trails that are perpendicular to *c* in [001] projection (Figures
211 1 and 4a, yellow arrows). Although not measured precisely, the trails appear to be normal to the
212 rhombohedral surfaces. This same orientation is observed in quartz crystals from other locations
213 that exhibit similar inclusions patters (e.g. Okada et al. 2017). These lineations make up the
214 trapiche-like patterns that generally follow the trigonal symmetry of the quartz crystal (Figure 1).
215 At 50X magnification in transmitted light, these dark-colored inclusions appear to be clumped,
216 tabular, or sheet-like crystals that are translucent and brownish to honey-green in color (Figure
217 4B, yellow arrow).
218
219 ***Identification of inclusions***
220 The XRD data indicate that the dark-colored inclusions (Figure 4, yellow arrows) are a
221 smectite clay mineral (Figure 5) similar to ferrosaponite (PDF 00-055-0982; Chukanov et al.
222 2003) or nontronite (PDF 00-34-0842; Eggleton 1977), or possibly vermiculite (PDF 04-017-
223 7291, Slade et al. 1985). Approximate chemical analyses of the inclusions by EDS produce
224 cation ratios of $(Ca_{0.24},Na_{0.07})(Fe_{1.29},Mg_{0.9},Al_{0.15},Mn_{0.09})Si_4$ (Supplementary Table 1). These
225 results align most closely with a smectite-type clay, such as a ferrosaponite ($Ca_{0.3}$
226 $(Fe^{2+},Mg,Fe^{3+},)_3\,(Si,Al)_4\,O_{10}\,(OH_2)\cdot 4H_2O$) or nontronite ($Ca_{0.5}\,(Si,Al,Fe)_8\,(Fe^{3+},Al,Mg)_4\,O_{20}$
227 $(OH)_4$).

This is the peer-reviewed, final accepted version for American Mineralogist, published by the Mineralogical Society of America.
The published version is subject to change. Cite as Authors (Year) Title. American Mineralogist, in press.
DOI: https://doi.org/10.2138/am-2021-7454. http://www.minsocam.org/

SEM micrographs showcasing the platy morphology of these inclusions further supports that these dark-colored inclusions are clay minerals (Figure 6) and is also consistent with *the in situ* optical observations (Figure 4B, yellow arrow). The convergent results suggest that these clay inclusions are not artifacts from the cutting and polishing process.

The fibrous inclusions (Figure 4, red arrows) are light-colored, less than 5 μm wide, and are identified as an amphibole, with the closest match to grunerite, via confocal Raman spectroscopy (Figure 7; Supplementary Table 2) by matching the most prominent non-quartz peak at approximately 670 $cm^{-1}$ (Figure 7, insert). The fibrous morphology of these inclusions is also consistent with grunerite and related amphibole minerals. These fibrous inclusions were not sufficiently abundant to be identified by X-ray diffraction. Optical images of the fibrous inclusions at high magnification indicate that they are not oriented in any particular direction within the quartz, but rather form a tangle of fibers (Figure 4c).

***Cathodoluminescence***

CL imaging across a quartz slice reveals internal heterogeneous growth features that are otherwise invisible by optical microscopy and backscattered electron imaging (Figure 8). In particular, a bright yellow CL band highlights former subcrystal outlines (Figure 8b). Superimposing the distributions of the clay inclusions over this CL image shows that the clay inclusions form a zone that begins at the termination of the initial stage of quartz growth (characterized by low CL intensity) and does not extend beyond the bright yellow CL band (Figure 8c).

High-resolution CL imaging of the yellow CL band (see blue boxed regions in Figure 8b) clearly shows the quartz sector boundaries (Figure 9a–c) and the straight crystal edges, as

opposed to the rough textures along the centers of former faces of the crystal (Figure 9d). Subcrystal boundaries and the inclusion of secondary phases leads to contrast at the buried subcrystal interfaces which is particularly evident in the high-magnification CL images (Figure 9c,d). Optical images in cross-polarized light also reveal heterogeneous growth features in these quartz slices which are consistent with our CL observations, such as the boundaries between sectors (Figures 8a, 9a,c).

### *Ti and Al measurements*

Trace concentrations of Ti and Al were measured via EPMA across a transect marked as a red line in Figure 8a,b, with specific values presented in Supplementary Table 3. Most Ti analyses across the transect were homogenous and below the 6 ppm (μg/g) detection limit. Aluminum concentrations were above the detection limit (6 ppm) and were heterogeneous across the transect (Figure 10). Comparison of Al concentration to the corresponding optical and CL images (see red transects on Figure 8), clearly shows how the lack of clay inclusions in the core region of the sample corresponds to high Al concentrations, followed by a rather sudden introduction of clay inclusions around the point on the sample where Al concentrations drop (Figure 10).

## Discussion

### Rough surface textures and the mechanical incorporation of inclusions

By combining our observations of exterior morphology and surface topography and interior quartz growth textures, we propose that rough surfaces mechanically trapped the

inclusions during growth that form the trapiche-like patterns in these quartz slices. The rough surface topography at the centers of the rhomboidal faces of the main quartz crystal is the result of the overlap and coalescence of subcrystals at the intersection of the rhomboidal faces and the prism faces of the main crystal. As is further discussed below, we suggest that these subcrystals arise from multiple growth centers during 2D nucleation and spread, and split crystal formation. Where multiple subcrystals meet, a depression is created where small grains of other minerals can collect and eventually be buried (incorporated) as the depression is filled through continued growth of the quartz. Such voids may trap secondary minerals or be filled with fluid (i.e. fluid inclusions). This is visible in a 2D slice of our CT scans where we see an unfilled void (Figure 3e, white arrow). Inclusion distributions influenced by rough surface topography during growth have been seen in other minerals, for example in metamorphic garnets (Andersen 1984; Jamtveit and Andersen 1992). The hypothesis of texture-based clay adhesion is further supported by our observation of a small clay seam between the two merged trapiche-like patterns in the slice from the complete crystal specimen (Figure 2e, blue arrow on inset). The seam formed as clay was trapped in the reentrant between the terminations of the two intergrown crystals (Figure 2e, blue arrow). The 3D reconstruction of our CT scan shows how inclusion phantoms correspond to episodes during crystal growth when clay minerals preferentially adhered to the rough areas of the crystal faces and were buried as growth continued (Figure 2e).

**Growth by two-dimensional nucleation and spread**

Two mechanisms dominate layer growth in crystals. These are spiral growth and two-dimensional nucleation and spread (Chernov 1984; Sunagawa 2005; Andreassen and Emslie Lewis 2017). The latter mechanism dominates growth above a critical supersaturation where the

297 activation barrier to the formation of a surface nucleus is overcome. Because of the higher degree
298 of supersaturation, compared to the regime in which spiral growth dominates, the rate of crystal
299 growth is much greater. At the higher end of this growth regime hopper growth can occur
300 (Sunagawa 2005; Desarnaud et al. 2018). It has also been shown that split crystal development
301 can occur as a result of defect formation under advanced growth rates in such regimes
302 (Ul'yanova et al. 1984; Cha et al. 2013). In addition, foreign particles adsorbed on crystal
303 surfaces can serve as two-dimensional nucleation centers leading to crystal growth by this
304 mechanism at supersaturations below those predicted in clean systems (Liu et al. 1997; Liu
305 2001).

306 As two-dimensional nuclei grow larger, in both lateral and normal directions, individual
307 growth centers or islands may develop. The relief of surface topography resulting from this layer
308 growth mechanism is influenced by the relative rates of lateral and normal advance of growth
309 islands. When lateral advancement is dominant, growth islands coalesce leaving only a
310 microtopography, with macroscopically smooth surfaces. However, under certain conditions
311 islands continue to act as individual growth centers where normal advancement dominates,
312 sometimes referred to as polycentric crystal growth (Kvasnitsa et al. 1999). This can lead to
313 macroscopically rough surfaces with topographic textures resembling numerous subcrystals.
314 Although subcrystals morphologically appear to be individuals, because they are translationally
315 coherent with the main crystal at the atomic scale, they are still part of the larger crystal. In some
316 cases, subcrystals may develop an orientational offset from the main crystal, a phenomena
317 known as split crystal growth.

318

319 **Split crystal growth in quartz**

Split crystal growth was first recognized in natural systems and the characteristics of the resulting crystal morphologies have been extensively investigated. Split crystal morphologies range from smaller subcrystals "splitting" off-axis of one main crystal by a very small degree, to spherulites formed by increasing layers of split crystals oriented far from the original main crystal orientation (e.g. Grigor'ev 1961). Thus, a continuum of subcrystal offset exists from none at all, to many tens of degrees. Most early work published on split crystal morphology has been in the area of mineral ontogeny (Fersman 1935; Grigor'ev 1961; Maleev 1972; Petreus 1974; Grigor'ev and Zhabin 1975; Zhabin 1979; Ul'yanova et al. 1984). Although various causes and mechanisms of split crystal growth were proposed in earlier literature, recent application of analytical techniques with molecular and atomic scale resolution have provided new insights into the causes of split crystal growth, which are discussed below. Recent interest in split crystal growth stems from a desire to synthetically grow crystals and crystal aggregates with complex morphologies for potential materials applications, and to better understand crystal growth during biomineralization (Cölfen and Antonietti 2005).

The morphologies of the quartz crystals in this study suggest that they grew by a type of crystal splitting mechanism (Grigor'ev 1961; Ul'yanova et al. 1984), sometimes referred to as block, mosaic, or lineage structure growth (Buerger 1932; Petreus 1978; Rykart 1995). The habit of the main crystal with divergent subordinate crystals in this specimen is similar and related to so-called "artichoke quartz," but without the strong widening effect of the split crystal typically observed in artichoke quartz growth or Sprossenquarz (Stalder 1976; Rykart 1995; Akhavan 2013). Interestingly, many other minerals found in the Huanggang deposit also show related split crystal morphologies, including arsenopyrite, borcarite, calcite, garnet, helvine, and ilvaite (Ottens and Neumeier 2012). This may suggest that crystal splitting morphologies could be

343 indicative of the environmental conditions of this deposit known to potentially cause crystal
344 splitting, such as high levels of molecular-scale impurities in the formation fluid and/or high
345 degrees of supersaturation that causes rapid crystal growth. We speculate that the smooth regions
346 of the rhombohedral faces, near their edges (Figures 2d & 3a, red arrows), may be the result of
347 faster growth and filling of coalescence pits in this region due to the Berg effect of steeper
348 diffusion gradients around the rhombohedral edges (Berg 1938; Sunagawa 2005).

349 The growth mechanism and cause of split crystals under natural conditions is poorly
350 understood (Grigor'ev 1961; Ul'yanova et al. 1984). Recent studies of the morphologies of
351 synthetic nanocrystals has shown that splitting can result from several different causes. These
352 include the incorporation of molecular-scale impurities that cause offsets in the crystal structure
353 (Pilapong et al. 2010); poor orientation fidelity during crystal growth by self-assembly of
354 nanoparticles (Tang and Alivisatos 2006; Suzuki et al. 2015; Arumugam et al. 2017); and
355 systematic defect production during rapid crystal growth at high degrees of solution
356 supersaturation (Cha et al. 2013). In the quartz specimens examined in this study, we observe
357 that the earliest stage of crystal growth produced transparent quartz (corresponding to the lower
358 section of the crystal in Figure 2A), which is also observed in slices reported by Laurs (2016).
359 The onset of crystal splitting in our quartz specimens appear to correlate with the growth of
360 translucent, milky quartz which suggests that the splitting could also have led to micro- or nano-
361 sized fluid inclusions that scatter light and lead to a translucent diaphaneity. This observation of
362 a clear core preceding split growth in quartz is consistent with another quartz example from the
363 Khingansk deposit, Russia, described by Grigor'ev (1961) in their Figure 81. The correlation
364 between crystal splitting morphology and turbid quartz and/or healed fractured quartz is
365 observed across other localities as well (Akhavan 2013).

This is the peer-reviewed, final accepted version for American Mineralogist, published by the Mineralogical Society of America.
The published version is subject to change. Cite as Authors (Year) Title. American Mineralogist, in press.
DOI: https://doi.org/10.2138/am-2021-7454. http://www.minsocam.org/

366

367 **Trapiche and Trapiche-like internal structures**

368 The term trapiche was first used in mineralogy to describe the morphology of unusual
369 emerald crystals from Columbia, and comes from the Spanish word for the cogwheels used in
370 processing sugar cane, which the emerald morphology resembles (Nassau and Jackson 1970). A
371 comprehensive review of trapiche emeralds and a detailed formational model is given by
372 Pignatelli et al. (2015). The trapiche morphology and specific internal textural characteristics,
373 including distinct sector boundaries within coherent single crystals resulting from a high density
374 of inclusions along those boundaries, has been observed in other minerals including andalusite
375 (chiastolite variety; Rice and Mitchell, 1991; Rice, 1993), garnets (Harker, 1950; Atherton and
376 Brenchley, 1972; Wilbur and Ague, 2006), corundum (Müllenmeister and Zang, 1995;
377 Schmetzer et al., 1996, 1998; Sunagawa, 1999; Garnier et al., 2002a, 2002b), and tourmaline
378 (Hainschwang et al., 2007; Schmetzer et al., 2011).

379 Heterogeneously distributed, but crystallographically controlled, inclusions that differ
380 from those found in trapiche emeralds, and other textural characteristics such as those in the
381 complex intergrowths of cordierite and indialite (Rakovan et al. 2006) can lead to specimens
382 with star-like patterns that have also been characterized as trapiche (Pignatelli et al. 2015;
383 Bohannon 2019). Because of the distinct differences in formation mechanisms between these
384 minerals' inclusion patterns and trapiche emeralds, Schmetzer et al. (2011) used the term
385 "trapiche-like" to characterize their internal morphologies. The quartz crystals in this study
386 exhibit a trapiche-like internal texture.

387

388 **The physicochemical context for trapiche-like quartz formation**

This is the peer-reviewed, final accepted version for American Mineralogist, published by the Mineralogical Society of America.
The published version is subject to change. Cite as Authors (Year) Title. American Mineralogist, in press.
DOI: https://doi.org/10.2138/am-2021-7454. http://www.minsocam.org/

389 Heterogeneity in the growth history of this crystal as evidenced by CT scans (Figure 7b),
390 CL images (Figure 8b), and optical images in cross-polars (Figure 8a), likely represents variable
391 chemical and/or temperature conditions during the quartz growth history that may have also
392 impacted the distribution of the clay inclusions (Figure 8c). A compositional profile within one
393 of the quartz slices offers clues about fluid chemistry as the quartz formed. Specifically, EPMA
394 was utilized to measure concentrations of aluminum and titanium across the sample section that
395 was imaged with CL (Figure 8, red transects). $Al^{3+}$ is incorporated into the quartz structure as a
396 substitution for $Si^{4+}$. Due to the difference in charge, this substitution must be balanced with the
397 addition of a monovalent cation (e.g., $Li^{+}$, $Na^{+,}$ $K^{+}$, $H^{+}$), usually on an interstitial site in the
398 structure, or with $P^{5+}$ ($2Si^{4+} = Al^{3+} + P^{5+}$). Previous work has demonstrated that $H^{+}$ is the
399 dominant cation responsible for charge-balancing $Al^{3+}$ in non-magmatic systems, and that the
400 amount of $Al^{3+}$ in the quartz varies as a function of fluid composition (e.g, pH, buffering mineral
401 assemblage) at the time of quartz crystallization (Merino et al. 1989; Jourdan et al. 2009;
402 Potrafke et al. 2019). Thus, variations in Al concentrations in quartz can function as a qualitative
403 proxy for changes in the fluid during quartz growth. For example, all other factors being equal,
404 the substitution mechanism $Si^{4+} = Al^{3+} + H^{+}$ suggests that increasing the activity of $H^{+}$ (pH) in
405 the system would induce increased aluminum solubility (Perny et al. 1992). Conversely,
406 increasing pH has been shown to stabilize tetrahedral $Al^{3+}$ in aqueous fluids, which could also
407 account for an increase in Al solubility in quartz (Merino et al. 1989). Finally, the presence of a
408 mineral phase that changes the partitioning of Al between quartz and the fluid (e.g., amphibole,
409 clays) could alter the solubility of Al in quartz. We suggest that variations in Al content along the
410 transect (Figure 10) correspond to changes in the chemistry of the fluid from which the quartz is
411 crystallizing.

This is the peer-reviewed, final accepted version for American Mineralogist, published by the Mineralogical Society of America.
The published version is subject to change. Cite as Authors (Year) Title. American Mineralogist, in press.
DOI: https://doi.org/10.2138/am-2021-7454. http://www.minsocam.org/

Although the complexity of the system precludes specific interpretations of the cause of the correlation between the presence of clays and Al content in the quartz, pH could play a significant role. For example, the appearance of clay inclusions could occur due to an increase in pH stabilizing the clays in the solution from which the quartz crystallized (e.g., McBride 1994). In turn, the increase in pH would diminish the solubility of Al in the quartz. In summary, the incorporation of Al into the quartz structure is heterogeneous across the sample and likely reflects shifts in formation fluid chemistry. This heterogeneity in the chemical history of the formation fluid may also explain the heterogeneity in the presence of inclusions that we observe across the length of the complete crystal sample (Figure 3b). Future research on the interplay between fluid composition and Al solubility in quartz could provide valuable information on the evolution of these and other important systems (e.g., porphyry copper and gold deposits).

Similar to $Al^{3+}$, $Ti^{4+}$ also readily substitutes for $Si^{4+}$ in the quartz structure. Titanium concentrations in quartz are sensitive to temperature, pressure, and the activity of Ti ($a_{TiO2}$) in the system at the time of quartz crystallization. The influence of these three variables on Ti solubility in quartz has been experimentally calibrated (Thomas et al. 2010) such that measuring Ti concentrations in a system with reasonable constraints on pressure and $a_{TiO2}$ can provide an estimate of crystallization temperature. Ti-in-quartz thermobarometry is widely utilized in igneous metamorphic systems to constrain crystallization temperatures. Here we measured Ti concentrations along the same transect as we did for Al to find that Ti concentrations are very low and relatively constant across the transect. This indicates that the temperature of formation was quite low, especially since Ti concentrations were at or below the detection limit (6 ppm Ti) along most of the transect. Some analyses recorded Ti contents of up to 18 ppm Ti. Using the Ti-in-quartz thermometer of Thomas et al. 2010 and assuming a crystallization pressure of 0.5 kbar

This is the peer-reviewed, final accepted version for American Mineralogist, published by the Mineralogical Society of America.
The published version is subject to change. Cite as Authors (Year) Title. American Mineralogist, in press.
DOI: https://doi.org/10.2138/am-2021-7454. http://www.minsocam.org/

435 (Mei et al., 2015) and $a_{TiO2} \approx 1$, 18 ppm Ti corresponds to a maximum crystallization
436 temperature of 410 °C. However, since most analyses were below the 6 ppm detection limit, the
437 majority of the quartz likely formed at temperatures below 348 ± 10 °C—the maximum
438 crystallization temperature based on 6 ppm Ti. This falls within the wide range of fluid inclusion
439 temperatures of entrapment for the Huanggang deposit, and falls within the sulfide stage of
440 mineralization (159−348°C) or at the transition between the oxide and sulfide stages defined by
441 Mei et al. (2015). We observed L-type fluid inclusions in the quartz, which suggests formation
442 temperatures between (192−348°C) in the sulfide stage (Mei et al. 2015). Chlorite
443 geothermometry also indicates that the later stage of mineralization at Huanggang No. 3 Mine
444 occurred at temperatures near 300°C (Wang et al. 2001). This temperature range falls at the
445 lower end of the 250 to 500°C temperature range observed to form other tin skarn deposits
446 worldwide (Kwak and Askins 1981; Dobson et al. 1982; Layne and Spooner 1991; Layne et al.
447 1991; Meinert 1992). The dominant yellow CL signal observed in the quartz (Figure 8b) is also a
448 qualitative indication crystallization temperature, as yellow CL is commonly observed in agates
449 and lower-temperature acidic volcanic hydrothermal vein quartz. Contrastingly, in magmatic and
450 solid-state metamorphic quartz, blue, red and violet CL signals dominate the spectra (Götze et al.
451 1999, 2001, 2015). Any potential variations in crystallization temperature could also influence
452 Al solubility in the quartz, although these variations are likely small relative to the contribution
453 of changes in fluid chemistry (Dennen et al. 1970).
454
455 **Implications**
456

This study on the mechanism of formation trapiche-like quartz showcases how crystal growth can impact the distribution of inclusions within a crystal in a natural system and it may serve to inspire works in materials science. Split crystal growth is currently an active topic of research in materials science for the purposes of making new nanomaterials, such as branching nano-crystals and for applications in biomimetics. The formation of these unique trapiche-like patterns in quartz is also of particular interest to the lapidary and gem industries.

Our work explores how split crystal growth is manifested in a natural system and on a larger scale. Considering that split crystal growth is observed in quartz from other deposits worldwide and in many other mineral species in the Huanggang deposit, split growth is a common phenomenon that could potentially be utilized as a geological indicator for the presence of abundant molecular scale impurities and/or highly supersaturated conditions in the formation fluid. Our chemical analyses of Ti concentrations and our observations of fluid inclusions suggests that this example of split crystal growth occurred at relatively low temperatures (<350°C). Further research will be required to pinpoint which conditions (formation temperatures, crystal growth rates) may be reliably inferred from observing split crystal growth morphologies in a geological deposit.

Aluminum chemical analyses and CL imaging suggest that the quartz grew from a fluid with a heterogeneous chemical and/or temperature history that correlates with the presence of clay inclusions. This heterogeneity in growth history is also reflected in previous studies that have observed that the onset of crystal splitting in milky regions of quartz follows a clear core. Our study demonstrates that not only does split crystal growth incorporate the nano- to micron-scaled inclusions that cause the milky turbidity in quartz, but that it can also pick up larger, millimeter-scaled inclusions, such as clays. Our novel use of micro-CT scanning to observe the

480 distributions of these inclusions within milky quartz also opens up new possibilities for using this
481 technique in future mineralogical studies.
482
483
484 **Acknowledgements**

485 The authors would like to thank Bert Ottens for his insights on the Huanggang Mine in Inner
486 Mongolia, China, the Smithsonian Institution Department of Mineral Sciences for the quartz
487 samples, Greg Polley for photographing the quartz slices, Rob Wardell for slicing the samples
488 and for help with the luminoscope (CL) technique, and JJ Hill for aiding with the micro- X-ray
489 CT scanning. We are grateful to Amir Akhavan and Associate Editor Maarten Broekmans
490 for their detailed reviews and suggestions to improve this manuscript. Funding for G.F. and for
491 this project was made possible by a Smithsonian Peter Buck Postdoctoral Fellowship and the
492 Coralyn W. Whitney Curator Endowment.
493
494 **References**

495 Andersen, T. B. (1984) Inclusion patterns in zoned garnets from Magerøy, north Norway.
496 Mineralogical Magazine, 48, 21−26.
497
498 Andreassen, J.P., and Emslie Lewis, A. (2017) Classical and nonclassical theories of crystal
499 growth, p.137−154. In A.E.S. Van Driessche, M. Kellermeier, L.G. Benning, and D. Gebauer
500 Eds., New Perspectives on Mineral Nucleation and Growth from Solution Precursors to Solid
501 Materials, Springer, Berlin.
502

503 Akhavan, A. (2013) The Quartz Page (Online). Available: http://www.quartzpage.de/index.html
504 (accessed October 19, 2020).
505
506 Arumugam, D., Thangapandian, M., Linu, J., Mathavan, J., Jayaram, A., Palanichamy, M.,
507 Chandrasekaran, S.S., Subramanian, U., Gupta, M., Okram, G.S., and others (2017) Growth
508 mechanism of pine-leaf-like nanostructure from the backbone of $SrCO_3$ nanorods using LaMer's
509 surface diffusion: Impact of higher surface energy ($\gamma$ = 38.9 eV/nm$^2$) {111} plane stacking along
510 ⟨110⟩ ($\gamma$ = 3.4 eV/nm$^2$) by first-principles calculations. Crystal Growth and Design, 17,
511 6394−6406.
512
513 Atherton M.P., and Brenchley P.J. (1972) A preliminary study of the structure, stratigraphy and
514 metamorphism of some contact rocks of the Western Andes, near the Quebrada Venado Muerto,
515 Peru. Geological Journal, 8, 161–178.
516
517 Berg, W.F. (1938) Crystal growth from solution. Proceedings of the Royal Society of London,
518 Series A, 164, 79–95.
519
520 Bohannon, S. (2019) Emerald: The superstar of trapiche gemstones. Gemological Institute of
521 America https://www.gia.edu/gia-news-research/emerald-superstar-trapiche-gemstones.
522 Accessed July 29, 2020.
523
524 Buerger, M.J. (1932) The significance of "block structure" in crystals. American Mineralogist,
525 17, 177−191.

Cha, S.I., Hwang, K.H., Kim, Y.H., Yun, M.J., Seo, S.H., Shin, Y.J., Moon, J.H., and Lee, D.Y. (2013) Crystal splitting and enhanced photocatalytic behavior of $TiO_2$ rutile nano-belts induced by dislocations. Nanoscale, 5, 753−758.

Chernov, A.A. (1984) Modern Crystallography III: Crystal Growth, 517 p. Springer, Berlin.

Chukanov, N.V., Pekov, I.V., Zadov, A.E., Chukanova, V.N., and Mökkel, S. (2003) Ferrosaponite $Ca_{0.3}(Fe^{2+}, Mg, Fe^{3+})_3 (Si, Al)_4 O_{10}(OH)_2 \cdot 4H_2O$, the new trioctahedral smectite. Zapiski Vserossiyskogo Mineralogicheskogo Obshchestva, 132(2), 68−74.

Cölfen, H., and Antonietti, M. (2005) Mesocrystals: Inorganic superstructures made by highly parallel crystallization and controlled alignment. Angewandte Chemie, 44, 5576−5591.

Dennen, W.H., Blackburn, W.H., and Quesada, A. (1970) Aluminum in quartz as a geothermometer. Contributions to Mineralogy and Petrology, 27, 332−342.

Desarnaud, J., Derluyn, H., Carmeliet, J., Bonn, D. and Shahidzadeh, N. (2018) Hopper growth of salt crystals. The Journal of Physical Chemistry Letters, 9, 2961−2966.

Dobson, D.C. (1982) Geology and alteration of the Lost River tin-tungsten-fluorine deposit, Alaska. Economic Geology, 77, 1033−1052.

549 Eggleton, R. (1977) Nontronite: chemistry and X-ray diffraction. Clay Minerals, 12, 181.

550

551 Fersman, A.E. (1935) Achievements of Soviet Mineralogy and Geochemistry During Recent
552 Years, 1929−1934, Moscow-Leningrad, Izdatel'stvo A.N. SSSR. (in Russian).

553

554 Garnier V., Ohnenstetter D., Giuliani G., Blanc P., and Schwarz D. (2002a) Trace-element
555 contents and cathodoluminescence of "trapiche" rubies from Mong Hsu, Myanmar (Burma):
556 geological significance. Mineralogy and Petrology, 76, 179–193.

557

558 Garnier V., Ohnenstetter D., Giuliani G., and Schwarz D. (2002b) Rubis trapiches de Mong Hsu,
559 Myanmar. Revue de Gemmologie A.F.G., 144, 5–12.

560

561 Götze, J., Pan, Y., Stevens-Kalceff, M., Kempe, U., and Müller, A. (2015) Origin and
562 significance of the yellow cathodoluminescence (CL) of quartz. American Mineralogist, 100,
563 1469−1482.

564

565 Götze, J., Plötze, M., and Habermann, D. (2001) Origin, spectral characteristics and practical
566 applications of the cathodoluminescence (CL) of quartz–a review. Mineralogy and Petrology, 71,
567 225−250.

568

569 Götze, J., Plötze, M., Fuchs, H., and Habermann, D. (1999) Defect structure and luminescence
570 behaviour of agate–results of electron paramagnetic resonance (EPR) and cathodoluminescence
571 (CL) studies. Mineralogical Magazine, 63, 163d.

Grigor'ev, D.P. (1961) Ontogeny of minerals: Lvov, Izdatel'stvo L'vovskogo Univ. (in Russian), 250 p. English translation 1965, Israel Program for Scientific Translations, Israel.

Grigor'ev, D.P., and Zhabin, A.G. (1975) Ontogeny of Minerals: Individuals, 200 p. Nauka, Moscow (in Russian).

Hainschwang T., Notari F., and Anckar B. (2007) Trapiche tourmaline from Zambia. Gems & Gemology, 43, 36–46.

Harker A. (1950) Metamorphic Textures. Methuen and Co., London.

Ihinger, P.D., and Zink, S.I. (2000) Determination of relative growth rates of natural quartz crystals. Nature, 404, 865.

Jamtveit, B, and Andersen, T (1992) Morphological instabilities during rapid growth of metamorphic garnets. Physics and Chemistry of Minerals, 19, 176−184.

Jourdan, A-L., Vennemann, T.W., Mullis, J., Ramseyer, K., and Speirs, C.J. (2009) Evidence of growth and sector zoning in hydrothermal quartz from Alpine veins. European Journal of Mineralogy, 21, 219–231.

Krzemnicki, M.S., and Laurs, B.M. (2014) Gem Notes: Quartz with radiating fibres, sold as Trapiche quartz. Journal of Gemmology, 34(4), 296−298.

Kvasnitsa, V.N., Yatsenko, V.G. and Jaszczak, J.A. (1999) Disclinations in unusual graphite crystals from anorthosites of Ukraine. The Canadian Mineralogist, 37, 951–960.

Kwak, T.A.P., and Askins, P.W. (1981) Geology and genesis of the F-Sn-W (Be-Zn) skarn (wrigglite) at Moina, Tasmania. Economic Geology, 76, 439−467.

Lauf, R.J. (2012) A Collector's Guide to Quartz and Other Silica Minerals, 96 p. Schiffer Publishing Ltd, Atglen, PA.

Laurs, B.M. (2016) Gem Notes: Quartz slabs from Inner Mongolia. Journal of Gemmology, 35(1), 15.

Layne, G.D., and Spooner, E.T.C. (1991) The JC tin skarn deposit, southern Yukon Territory; I, Geology, paragenesis, and fluid inclusion microthermometry. Economic Geology, 86, 29−47.

Layne, G.D., Longstaffe, F.J., and Spooner, E.T.C. (1991) The JC tin skarn deposit, southern Yukon Territory; II, A carbon, oxygen, hydrogen, and sulfur stable isotope study. Economic Geology, 86, 48−65.

Liu, X.Y., Maiwa, K., and Tsukamoto, K. (1997) Heterogeneous two-dimensional nucleation and growth kinetics. Journal of Chemical Physics, 106, 1870−1879.

Liu, X.Y. (2001) New understanding for two-dimensional nucleation (II). Surface Review and Letters, 8, 423−428.

Maleev, M.N. (1972) Diagnostic features of spherulites formed by splitting of a single crystal nucleus. Growth mechanism of chalcedony: Tschermaks Mineralogische und Petrographische Mitteilungen, 18, 1−16.

McBride, M.B. (1994) Environmental Chemistry of Soils, 416 p. Oxford University Press, New York.

Mei, W., Lü, X., Cao, X., Liu, Z., Zhao, Y., Ai, Z., Tang, R., and Abfaua, M.M. (2015) Ore genesis and hydrothermal evolution of the Huanggang skarn iron–tin polymetallic deposit, southern Great Xing'an Range: Evidence from fluid inclusions and isotope analyses. Ore Geology Reviews, 64, 239−252.

Meinert, L.D. (1992) Skarns and skarn deposits. Geoscience Canada, 19, 145−162.

Merino, E., Harvey, C., and Murray, H.H. (1989) Aqueous-chemical control of the tetrahedral-aluminum content of quartz, halloysite, and other low-temperature silicates. Clays and Clay Minerals, 37, 135–142.

Müllenmeister H.J., and Zang J. (1995) Ein trapiche-rubin aus Myanmar (Burma). Lapis, 20(12), 50.

Nassau, K. (1968) On the cause of asterism in star corundum. American Mineralogist, 53, 300−305.

Nassau, K., and Jackson, K.A. (1970) Trapiche emeralds from Chivor and Muzo, Colombia. American Mineralogist, 55, 416−427.

Okada, T., Nagase, T., Imai, H., and Uehara, S. (2017). Sakura texture in quartz crystals from Obira mine, Oita prefecture, Japan. Japanese Magazine of Mineralogical and Petrological Sciences, 46, 117−123.

Ottens, B., and Neumeier, G. (2012) The Huanggang Mine Inner Mongolia, China. The Mineralogical Record, 43, 529−563.

Perny, B., Eberhardt, P., Ramseyer, K., Mullis, J., and Pankrath, R. (1992) Microdistribution of Al, Li, and Na in α quartz: Possible causes and correlation with short-lived cathodoluminescence. American Mineralogist, 77, 534−544.

Petreus, I (1974) The divided structure of crystals II. Secondary structures and habits. Neues Jahrbuch für Mineralogie, Abhandlungen (122/3): 314−338.

663 Petreus, I (1978) The divided structure of crystals I. Lineage and sectoral structure in
664 pyrite and beryl. American Mineralogist, 63, 725−731.
665
666 Pilapong, C., Thongtem, T., and Thongtem, S. (2010) Hydrothermal synthesis of double sheaf-
667 like Sb2S3 using copolymer as a crystal splitting agent. Journal of Alloys and Compounds, 507,
668 L38−L42.
669
670 Pignatelli, I., Giuliani, G., Ohnenstetter, D., Agrosì, G., Mathieu, S., Morlot, C., and Branquet,
671 Y. (2015) Colombian trapiche emeralds: Recent advances in understanding their formation.
672 Gems & Gemology, 51, 222–259.
673
674 Potrafke, A., Stalder, R., Schmidt, B.C., and Ludwig, T. (2019) OH defect contents in quartz in a
675 granitic system at 1–5 kbar. Contributions to Mineralogy and Petrology, 174, 11.
676
677 Rakovan, J., Kitamura, M., and Tamada, O. (2006): Sakura ishi (cherry blossom stones): mica
678 pseudomorphs of complex cordierite-indialite intergrowths from Kameoka, Kyoto Prefecture,
679 Japan. Rocks & Minerals, 81, 284−292.
680
681 Rakovan, J. (2009) Word to the Wise: Sectoral Zoning. Rocks & Minerals, 84, 171−176.
682
683 Rice A.H.N. (1993) Textural and twin sector-zoning and displacement of graphite in chiastolite
684 and -pyralspite and grandite garnets in the variscides of South-West England. Annual
685 Conference of the Ussher Society, 129–131.

Rice A.H.N., and Mitchell J.I. (1991) Porphyroblast textural sector-zoning and matrix displacement. Mineralogical Magazine, 55, 379–396.

Rykart, R. (1995) Quarz-Monographie - Die Eigenheiten von Bergkristall, Rauchquarz, Amethyst, Chalcedon, Achat, Opal und Anderen Varietäten. 2nd. Edition. Ott Verlag. Thun, Switzerland.

Schmetzer K., Hänni H.A., Bernhardt H.J., and Schwarz D. (1996) Trapiche rubies. Gems & Gemology, 32, 242–250.

Schmetzer K., Beili Z., Yan G., Bernhardt H.J., and Hänni H.A. (1998) Element mapping of trapiche rubies. Journal of Gemmology, 26, 289–301.

Schmetzer K., Bernhardt H.J., and Hainschwang T. (2011) Chemical and growth zoning in trapiche tourmaline from Zambia – a re-evaluation. Journal of Gemmology, 32, 151–173.

Slade, P.G., Stone, P.A., and Radoslovich, E.W. (1985). Interlayer structures of the two-layer hydrates of Na-and Ca-vermiculites. Clays and Clay Minerals, 33, 51−61.

Stalder, H.A. (1976) Flüssigkeits- und Gaseinschlüsse in Quarzkristallen Die Naturwissenschaften, 63, 449−456.

Sun, Z., Muyal, J. and Hand, D. (2018) Gem News International: Trapiche-like amethyst from Brazil. Gems & Gemology, 54(2), 237–238.

Sunagawa I. (1999) Growth and morphology of crystals. Forma, 14, 147–166.

Sunagawa, I. (2005) Crystals: Growth, Morphology, & Perfection, 295 p. Cambridge University Press, Cambridge, UK.

Suzuki, K., Tokudome, Y., Tsuda, H., and Takahashi, M. (2015) Morphology control of $BiFeO_3$ aggregates via hydrothermal synthesis. Journal of Applied Crystallography, 49, 168–174.

Tang, J., and Alivisatos, A.P. (2006) Crystal splitting in the growth of $Bi_2S_3$. Nano Letters, 6, 2701−2706.

Thomas, J.B., Watson, E.B., Spear, F.S., Shemella, P.T., Nayak, S.K., and Lanzirotti, A. (2010) TitaniQ under pressure: the effect of pressure and temperature on the solubility of Ti in quartz. Contributions to Mineralogy and Petrology, 160, 743−759.

Ul'yanova, T.P., Punin, Y.O., and Petrov, T.G. (1984) Trends in crystal splitting during growth. In: Chernov A.A. (ed) English translation, Consultants Bureau, New York/London. Growth of Crystals, 12, 135−140.

Vasconcelos, P., Wenk, H.R., and Rossman, G. (1994) The Anahí Ametrine Mine, Bolivia. Gems & Gemology, 30, 4−23.

Vertriest, W., Sangsawong, S., and Pardieu, V. (2016) Trapiche-type sapphire from Tasmania. Gems & Gemology, 52, 429−431.

Wang, L.J., Shimazaki, H., and Shiga, Y. (2001) Skarns and genesis of the Huanggang Fe-Sn deposit, Inner Mongolia, China. Resource Geology, 51, 359−376.

Webster, R. (1995) Gems, their Sources, Descriptions and Identification, 5th ed., 1072 p. Butterworths, London, UK.

Wilbur D.E., and Ague J.J. (2006) Chemical disequilibrium during garnet growth: Monte Carlo simulations of natural crystal morphologies. Geology, 34, 689–692.

Zhabin, A.G. (1979) Ontogeny of Minerals: Aggregates, 300 p. Nauka, Moscow (in Russian).

## Figure Captions

**Figure 1.** Slices of trapiche-like included quartz from Inner Mongolia, China are cut perpendicular to the *c*-axis of the crystal to highlight the symmetrical distributions of inclusions.

**Figure 2.** (**a**) An exterior view of a complete quartz specimen with two main crystals intergrown in sub-parallel orientation. The inclusions are visible as a grey zone beginning at the black arrows, about half-way up the specimen. Split crystals (heighted in white arrows) also emerge around this point, leading to an overall widening from the base (yellow bar width) to the top (red bar width) of the specimen. (**b**) The same quartz specimen from A was cut in half and photographed with a representative crystal slice exhibiting the internal trapiche-like patterns. (**c**) This image shows a close-up of the rough surface texture formed by numerous subcrystals on the prism faces. (**d**) The main crystal terminations show rough surface texture at the center of the rhombohedral faces (yellow arrows) and smooth, clean surfaces near the termination edges (red arrows). (**e**) A *c*-axis view of the quartz specimen with clay coating the rough central portions of the rhombohedral surfaces, mimicking the trapiche-like patterns we see in the slices. The blue arrow points to clay trapped between the two main crystal terminations, which may manifest itself as a seam in the slices (inset).

**Figure 3.** Micro-X-ray CT scans show 3-D renditions of quartz surface features and how inclusions are distributed within the quartz matrix to create trapiche- like patterns. (**a**) A surface rendition highlights the rough surface texture (yellow arrow) at the center of the rhombohedral faces compared to the smooth areas near the edges (red arrow). (**b**) A 3-D rendition of the inclusions (green) within the quartz shows that the inclusions are preferentially concentrated at different growth stages (concentric zones) as "phantoms" within the quartz crystal. These phantoms are most pronounced along planes parallel to the rhombohedral surfaces (**c**) X-ray CT renditions of the inclusions (green) in a section roughly parallel to (001) show the nuances in inclusion distributions, making them easier to view compared to optical images in Figures 1 and

8. (**d**) A higher magnification view of the inclusion trails in (**c**) show how they have rod- and sheet- like fabrics in three dimensions. The blue arrow indicates the fiber inclusions observed in Figure 4C. (**e**) A two-dimensional micro-CT slice in greyscale shows the lineations of inclusions (white trails, indicated by the green arrow), which lie adjacent to voids within the surrounding matrix (black dots, indicated by the white arrow).

**Figure 4.** Magnified images of inclusions in polarized transmitted light show (**a**) overall linear trails of dark inclusions (yellow arrows) within a quartz slice. (**b**) Individual, dark-colored clump inclusions (yellow arrow) and thin, colorless, fibrous inclusions (red arrow). (**c**) Fibrous inclusions are indicated with red arrows, and some dark, clump inclusions pointed to by yellow arrows.

**Figure 5.** X-ray diffraction measurements of the dark-colored inclusions were performed on (**a**) a section of one of the (001) quartz slices that was cut into fourths to better expose the dark-colored inclusions. X-rays were aimed at the darkest section (yellow circle). (**b**) 2D diffraction images were integrated between the discrete diffraction spots for quartz to isolate the signal from the dark-colored inclusions (yellow pie-slices). (**c**) Normalized X-ray diffraction patterns of the inclusions (black) best match patterns for ferrosaponite (green), nontronite (blue), and vermiculite (yellow) clay structures. Rescaled views of the minor peaks are represented in the lighter colors above the whole spectra.

**Figure 6.** Backscattered electron SEM micrographs of the dark-colored clump inclusions show platy, clay-like habits enveloped by the quartz.

**Figure 7.** Confocal micro-Raman spectroscopy measurements on fibrous inclusions (**a**−**c**) within the quartz. The Raman spectra are normalized to the maximum intensity value in each spectrum. The area inside of the grey inset box is a close-up of the region between 600−700 $cm^{-1}$ where a non-quartz peak ~670 $cm^{-1}$ indicates that the inclusions are likely an amphibole phase.

**Figure 8.** Internal morphology **(**crystal growth patterns) in a trapiche-like quartz slice visualized by (**a**) transmitted crossed-polarized light, highlighting crystallite inclusions, (**b**) cathodoluminescence (CL) accentuating concentric growth layers, and (**c**) transmitted plane-polarized light superimposed on the CL image showing the distribution of the inclusions within the quartz concentric zones. The added red lines in (**b**) and (**c**) represent the transect taken with the electron microprobe to measure trace elemental concentrations of Al and Ti (see Figure 10). The blue boxes in panel (**b**) represent the areas shown at higher magnification with CL in Figure 9.

**Figure 9.** High-magnification CL images of the brightest CL band in the quartz in Figure 8b show fine detail within these internal growth features, including sharp sector boundaries (**a**−**c**) and rough stepped faces (**d**) of the quartz where subcrystals coalesced as it grew.

**Figure 10.** Electron Microprobe analyses of Al concentrations across a transect following early- to late-stage growth in trapiche-like quartz. Errors as standard deviations are within the data point circles.

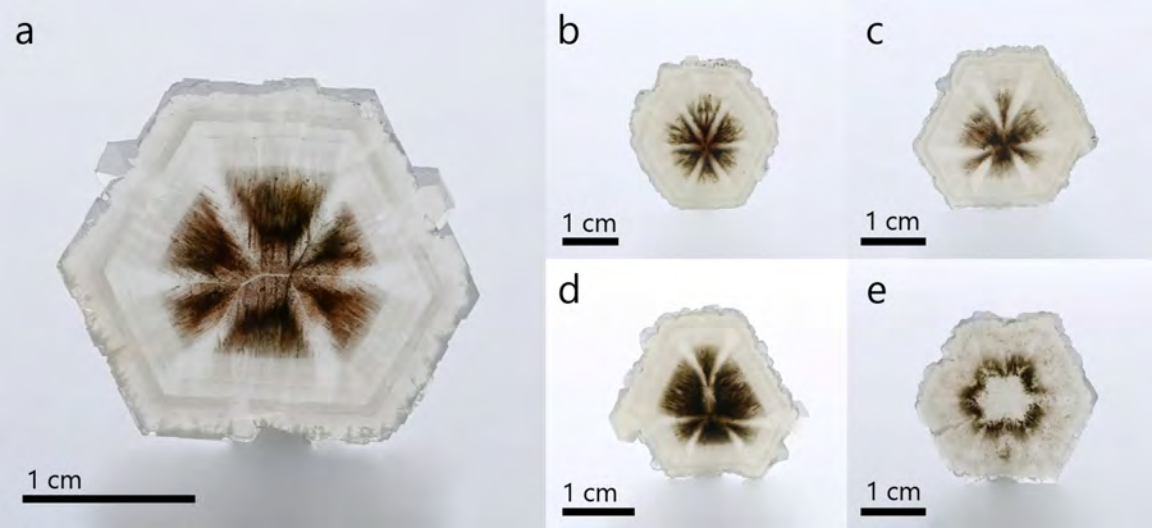
a
1 cm
b
1 cm
c
1 cm
d
1 cm
e
1 cm

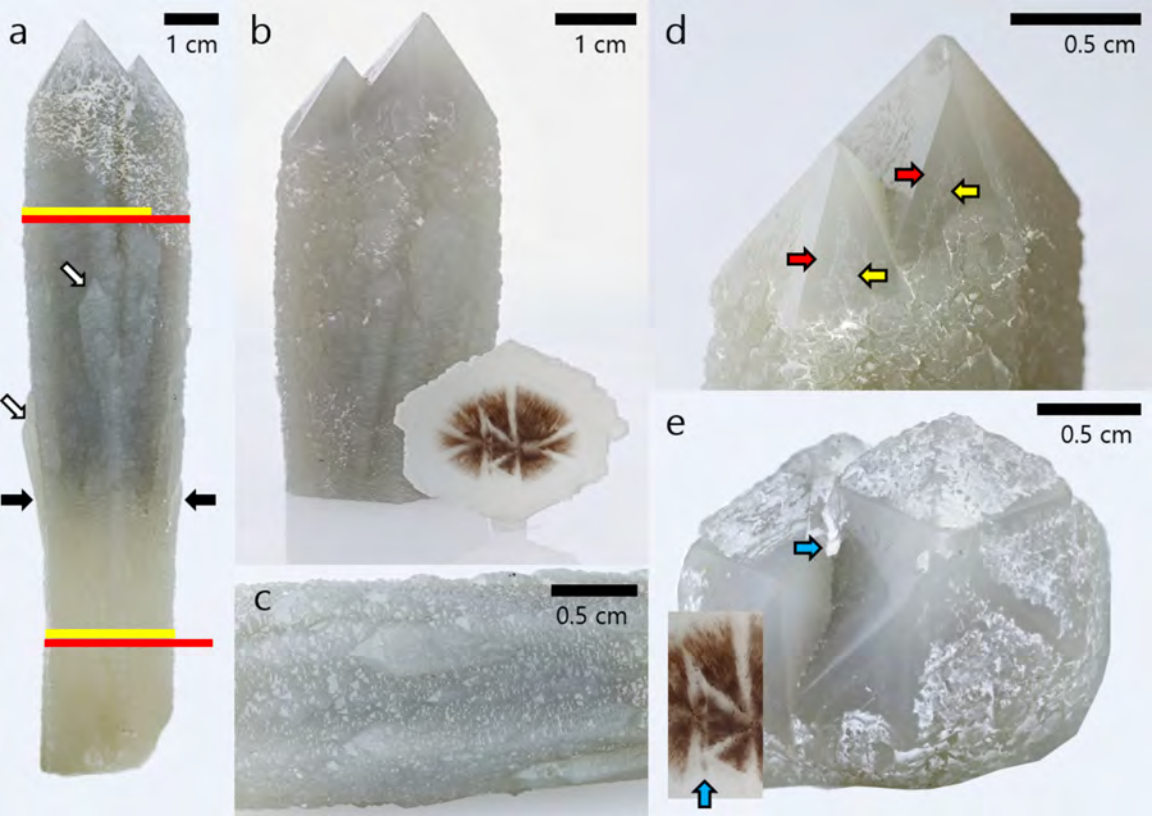
a
1 cm
b
1 cm
c
0.5 cm
d
0.5 cm
e
0.5 cm

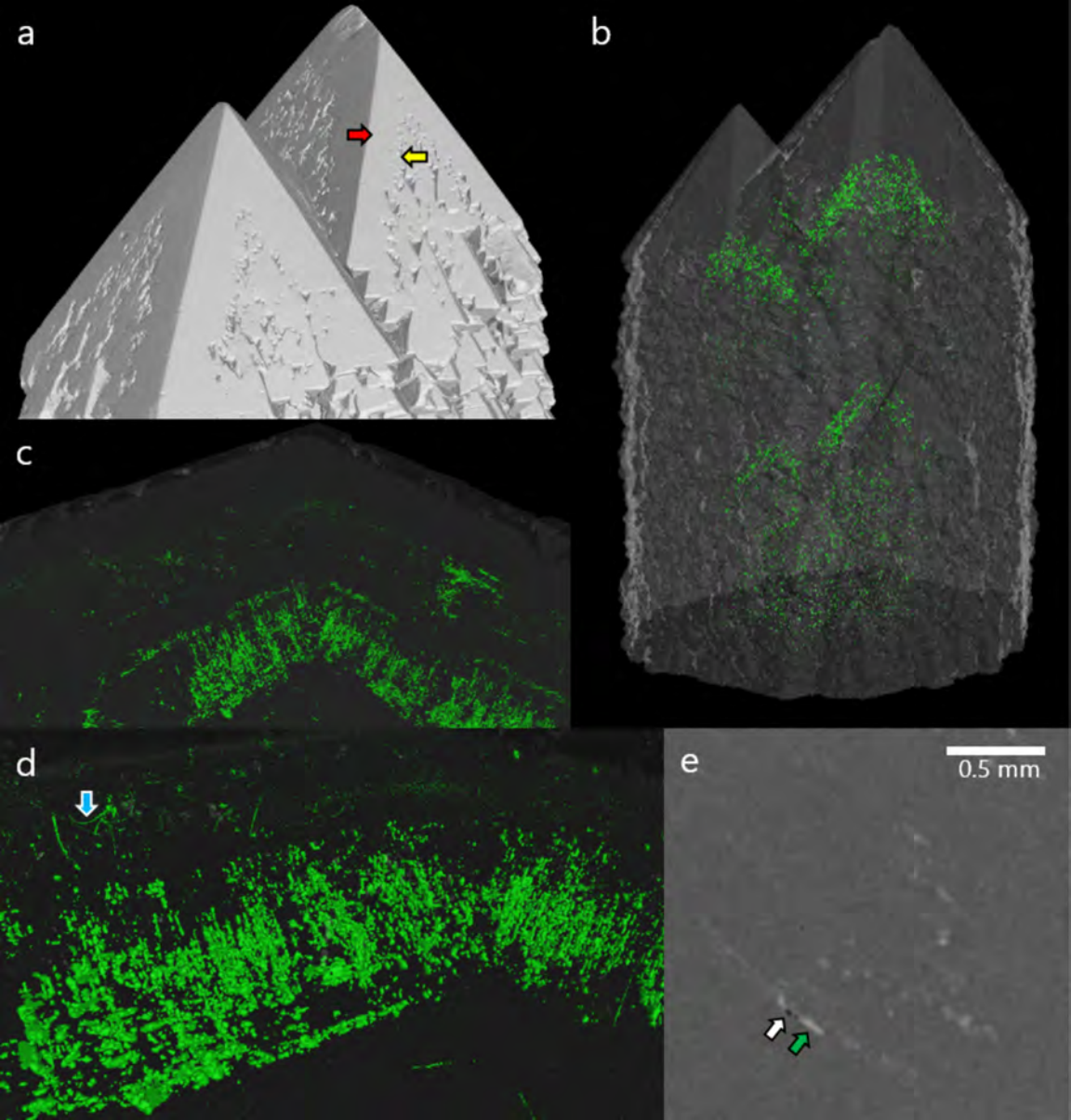
a
b
c
d
e
0.5 mm

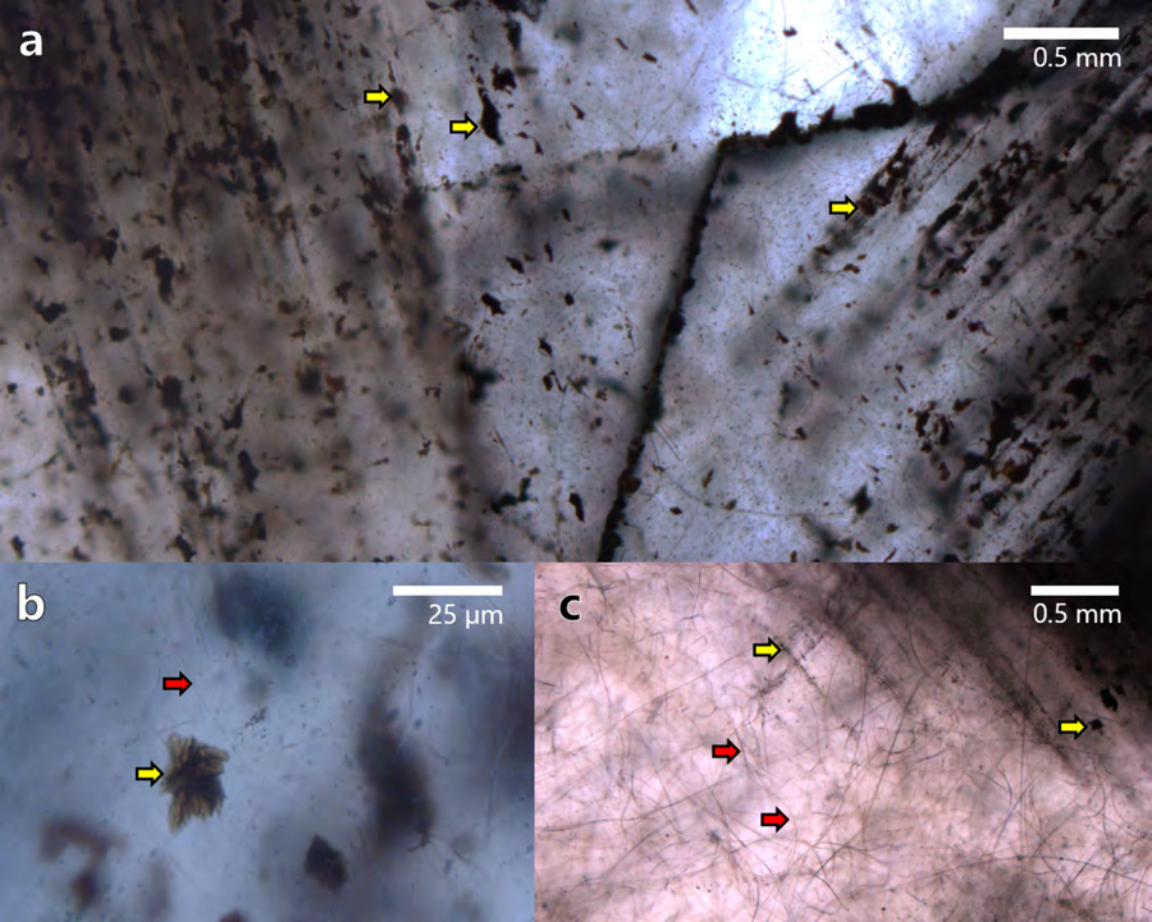
a
0.5 mm
b
25 µm
c
0.5 mm


a

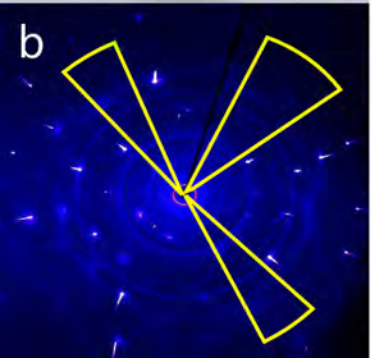
b

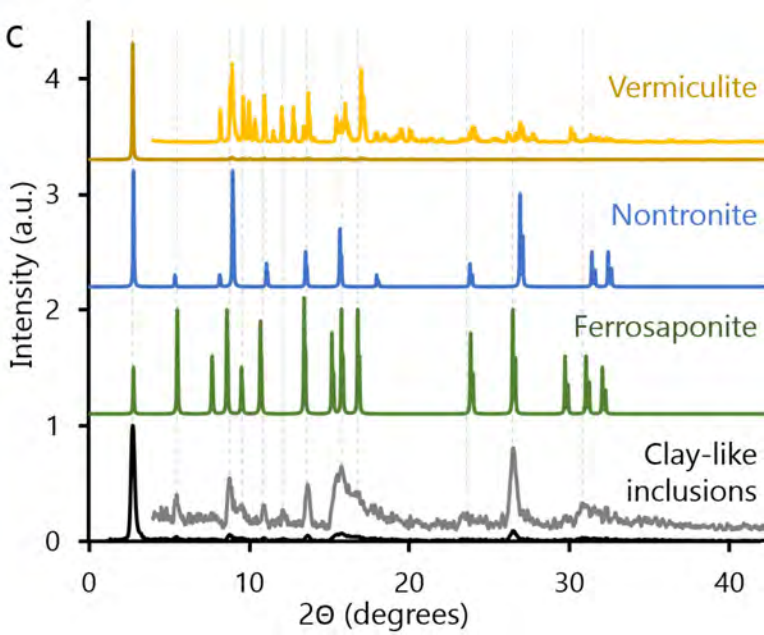
c
Vermiculite
Nontronite
Ferrosaponite
Clay-like
inclusions
Intensity (a.u.)
0
1
2
3
4
0
10
20
30
40
2Θ (degrees)

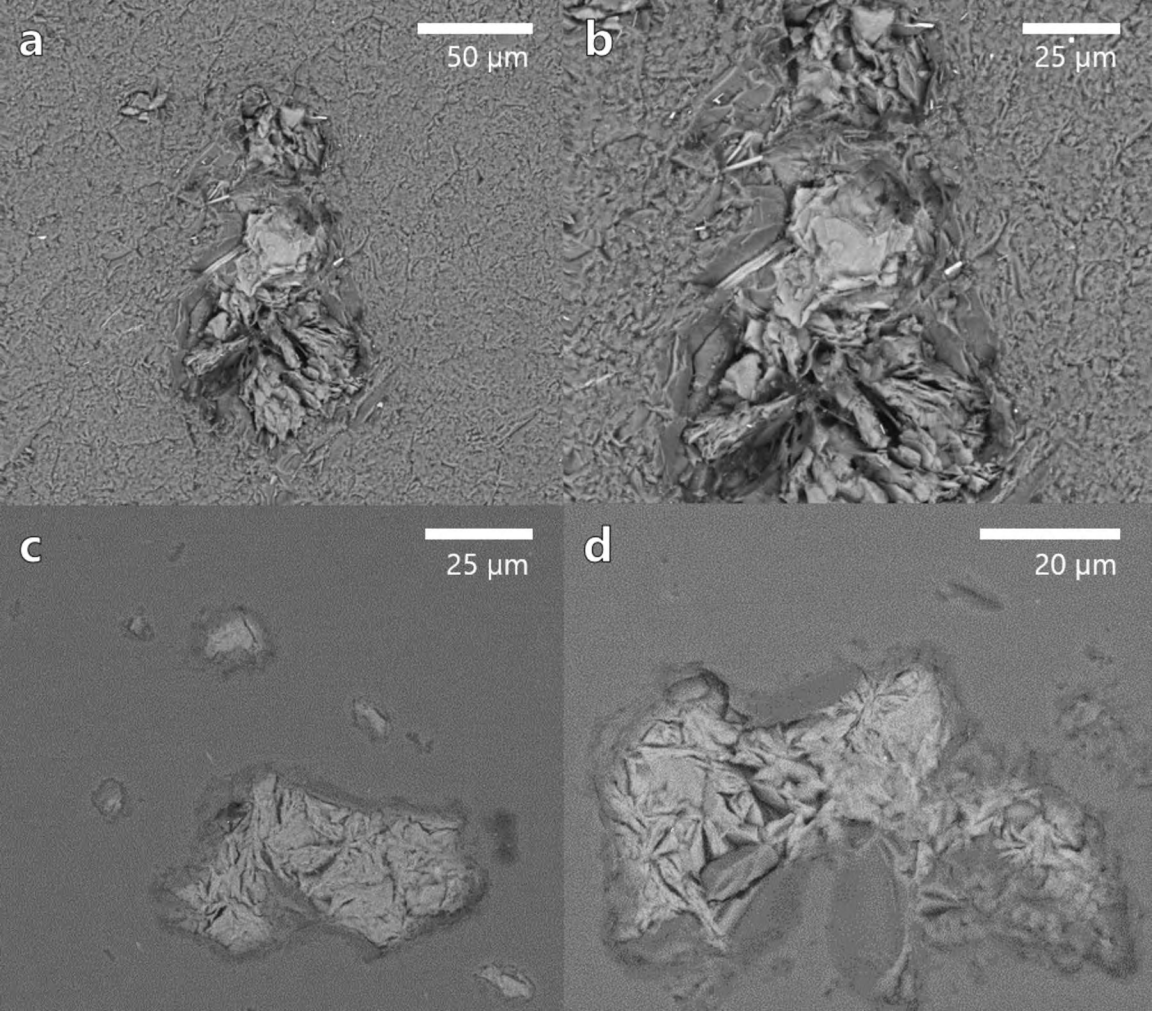
a
50 µm
b
25 µm
c
25 µm
d
20 µm

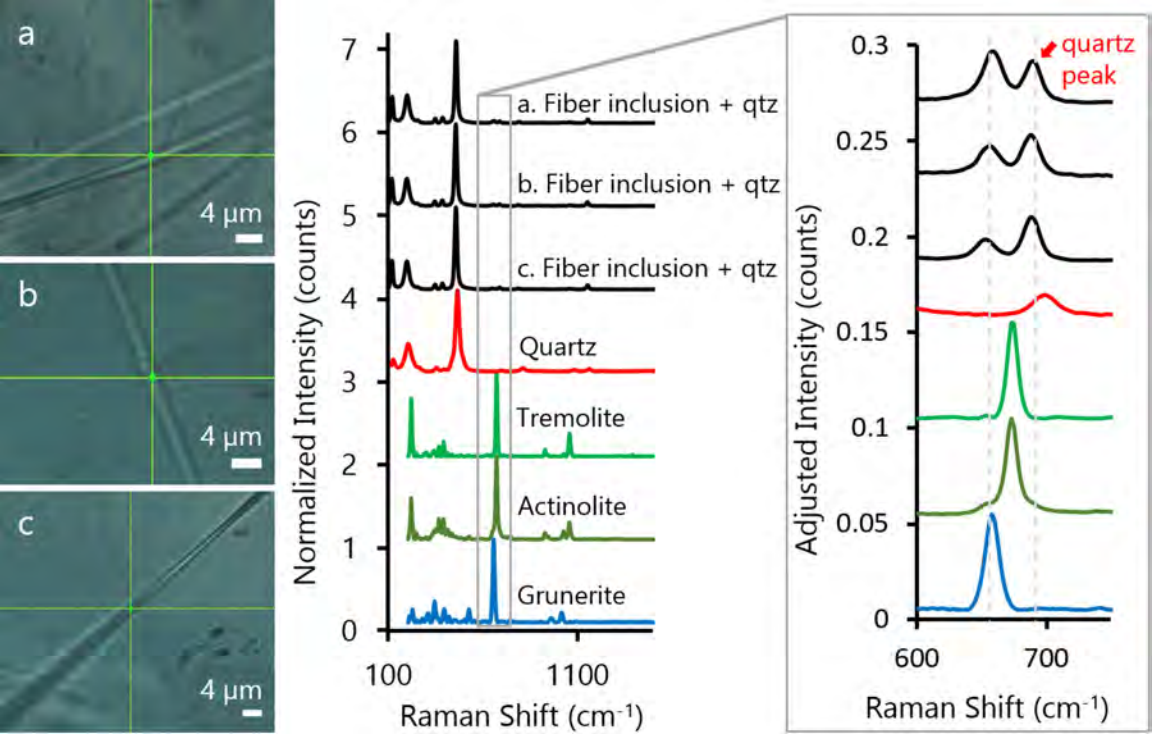
a
4 µm
b
4 µm
c
4 µm
Normalized Intensity (counts)
Raman Shift (cm⁻¹)
a. Fiber inclusion + qtz
b. Fiber inclusion + qtz
c. Fiber inclusion + qtz
Quartz
Tremolite
Actinolite
Grunerite
quartz peak
Adjusted Intensity (counts)
Raman Shift (cm⁻¹)

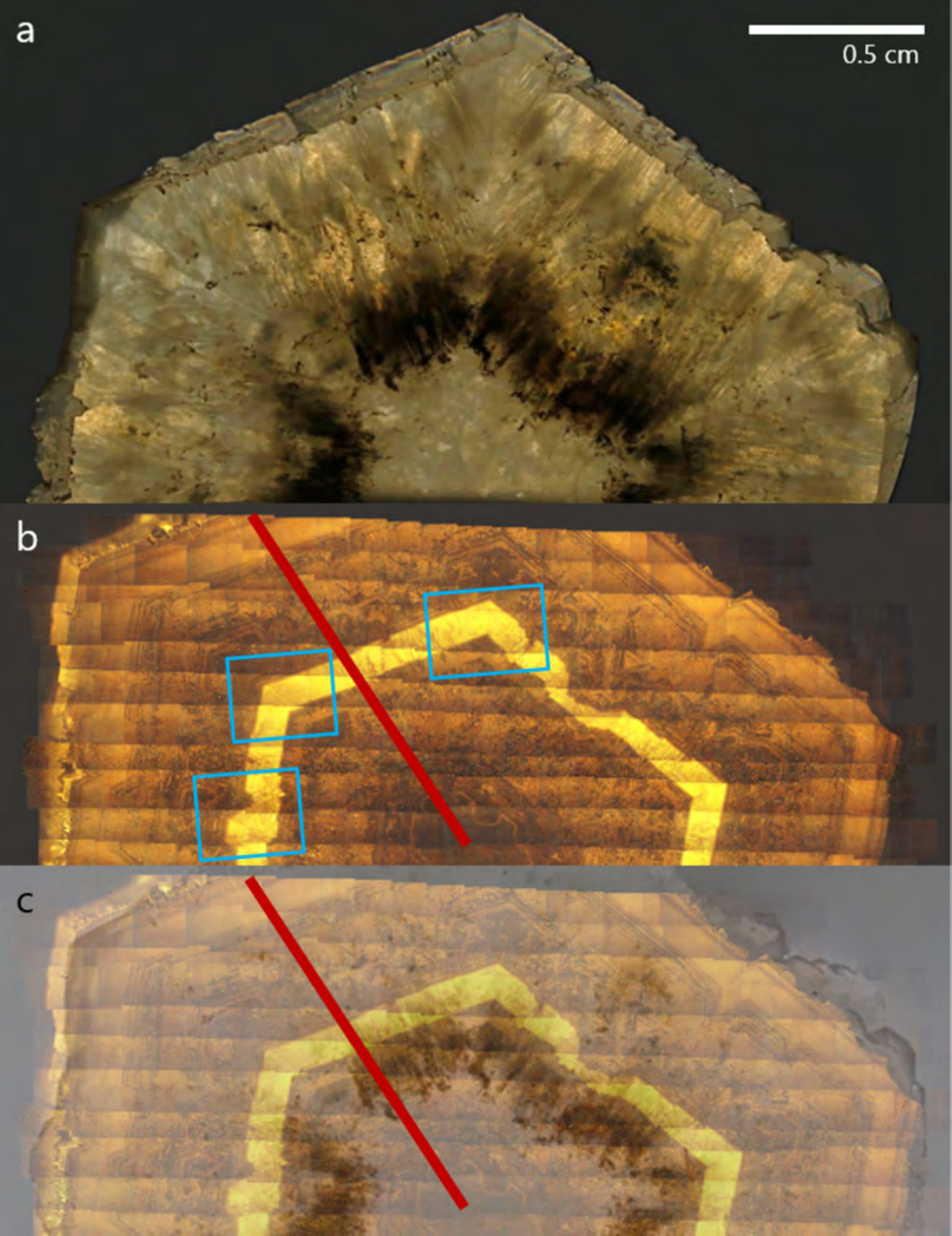
a
0.5 cm
b
c

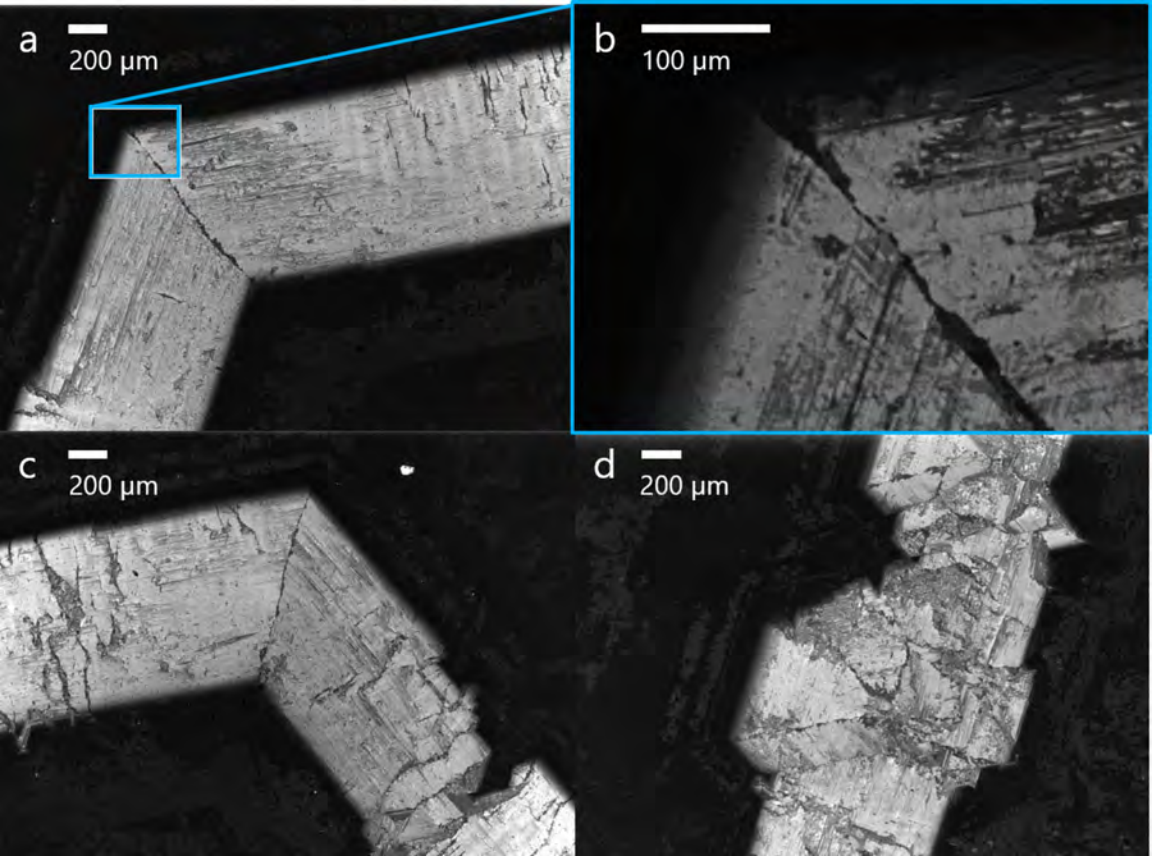
a
200 µm
b
100 µm
c
200 µm
d
200 µm

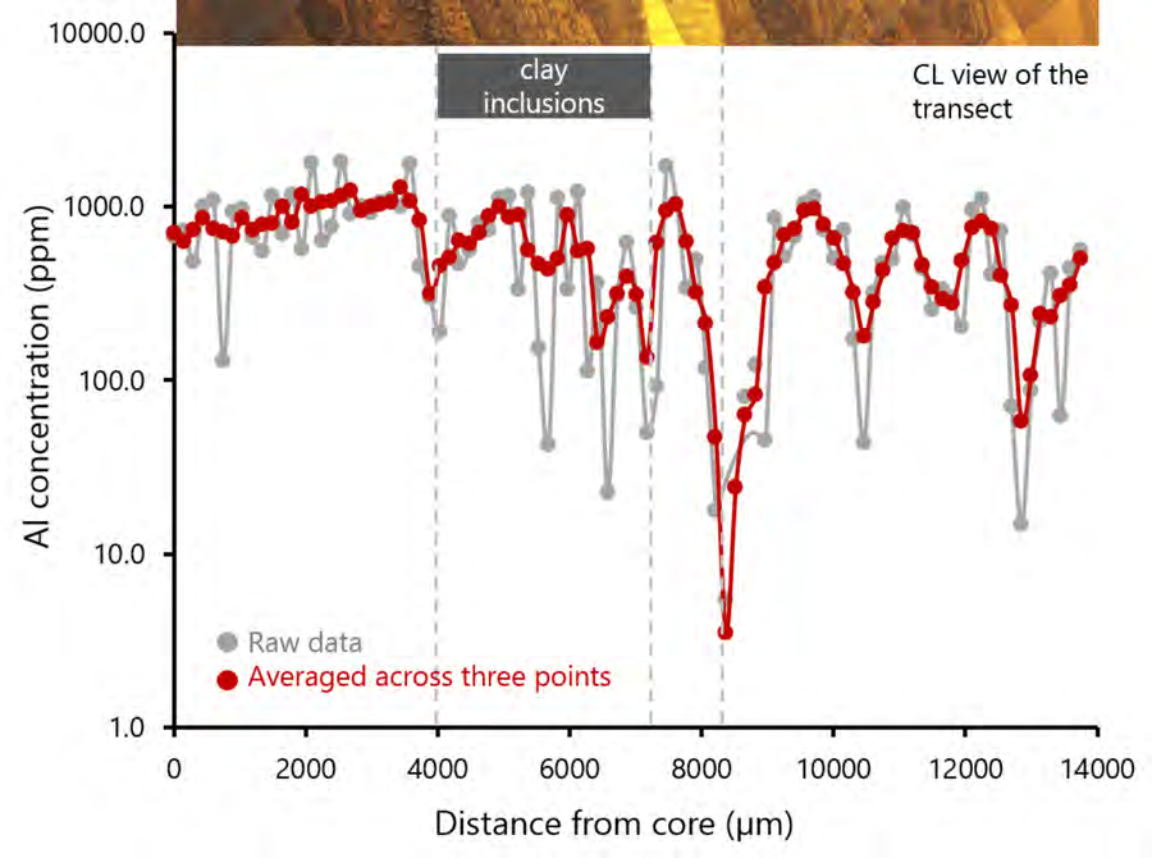
10000.0
clay inclusions
CL view of the transect
1000.0
100.0
10.0
1.0
Al concentration (ppm)
Raw data
Averaged across three points
0
2000
4000
6000
8000
10000
12000
14000
Distance from core (µm)